

Frequency Comb Generation via Cascaded Second-Order Nonlinearities in Microresonators

Jan Szabados¹, Danila N. Puzyrev,² Yannick Minet^{1,3}, Luis Reis¹, Karsten Buse^{1,4,*}, Alberto Villois,² Dmitry V. Skryabin^{2,†} and Ingo Breunig^{1,4}

¹Laboratory for Optical Systems, Department of Microsystems Engineering—IMTEK, University of Freiburg, Georges-Köhler-Allee 102, 79110 Freiburg, Germany

²Department of Physics, University of Bath, Bath BA2 7AY, United Kingdom

³Gisela and Erwin Sick Chair of Micro-optics, Department of Microsystems Engineering—IMTEK, University of Freiburg, Georges-Köhler-Allee 102, 79110 Freiburg, Germany

⁴Fraunhofer Institute for Physical Measurement Techniques IPM, Heidenhofstraße 8, 79110 Freiburg, Germany



(Received 18 February 2020; accepted 6 May 2020; published 22 May 2020)

Optical frequency combs are revolutionizing modern time and frequency metrology. In the past years, their range of applications has increased substantially, driven by their miniaturization through microresonator-based solutions. The combs in such devices are typically generated using the third-order $\chi^{(3)}$ nonlinearity of the resonator material. An alternative approach is making use of second-order $\chi^{(2)}$ nonlinearities. While the idea of generating combs this way has been around for almost two decades, so far only few demonstrations are known, based either on bulky bow-tie cavities or on relatively low- Q waveguide resonators. Here, we present the first such comb that is based on a millimeter-sized microresonator made of lithium niobate, that allows for cascaded second-order nonlinearities. This proof-of-concept device comes already with pump powers as low as 2 mW, generating repetition-rate-locked combs around 1064 and 532 nm. From the nonlinear dynamics point of view, the observed combs correspond to Turing roll patterns.

DOI: [10.1103/PhysRevLett.124.203902](https://doi.org/10.1103/PhysRevLett.124.203902)

Optical frequency combs are useful for applications such as precision spectroscopy in fundamental science [1,2], dual-comb spectroscopy [3], ultrafast distance measurements [4], Tbit/s telecommunications [4], and quantum information processing [5]. The range of applications has increased especially since stable solitonic combs were first demonstrated in microresonators in 2014 [6] and subsequently realized on a batch-compatible chip-integrated platform [7]. In total, however, it took almost a decade to get from first microresonator-based combs [8] to chip-integrated soliton combs. All these combs rely on third-order $\chi^{(3)}$ (Kerr) optical nonlinearities, which have thus been in the center of interest in recent years [4,9–12]. Solitonic Kerr combs are typically centered in the near infrared as they require anomalous dispersion at the pump frequency that is not readily available across the practically valuable visible part of the spectrum. An obvious solution to this is using a separate cavity with intrinsic $\chi^{(2)}$ nonlinearity to convert the initial comb via second-harmonic and sum-frequency generation [13]. One approach to simplify this is to use materials for Kerr-comb generation with intrinsic $\chi^{(2)}$ nonlinearity or to induce $\chi^{(2)}$ nonlinearity by, e.g., material-growth-induced stress [14], ion migration [15], or electric fields [16]. This way, one can generate a Kerr comb and convert it in a single cavity as demonstrated

in the $\chi^{(2)}$ materials aluminum nitride [17], gallium phosphide [18], and lithium niobate [19]. There is, however, another way to generate combs at the pump and second harmonic simultaneously based on $\chi^{(2)}$ nonlinearities only. This approach relies on cascaded $\chi^{(2)}$ -nonlinear optical processes, i.e., frequency doubling followed by optical parametric generation, again leading to frequency doubling and so on [20]. This process is intrinsically linked to comb generation around both the pump and second-harmonic frequencies (e.g., [21]). Furthermore, it promises to provide lower pump thresholds since for continuous-wave light the $\chi^{(2)}$ nonlinearity is generally much stronger than the third-order one. Although the idea has been around for almost two decades, so far only few experimental realizations are known, based either on bulky bow-tie cavities [22–26] or on relatively low- Q waveguide resonators [27], but none in high- Q microresonators.

Below we present the first frequency comb generated using cascaded second-order nonlinearities in a millimeter-sized ultrahigh- Q microresonator made of 5% MgO-doped z cut congruent lithium niobate and pumped with continuous-wave near-infrared laser light. If the pump light is ordinarily (o) polarized and the birefringence-phase-matching condition for second-harmonic generation is fulfilled, extraordinarily (e) polarized second-harmonic light is generated [28].

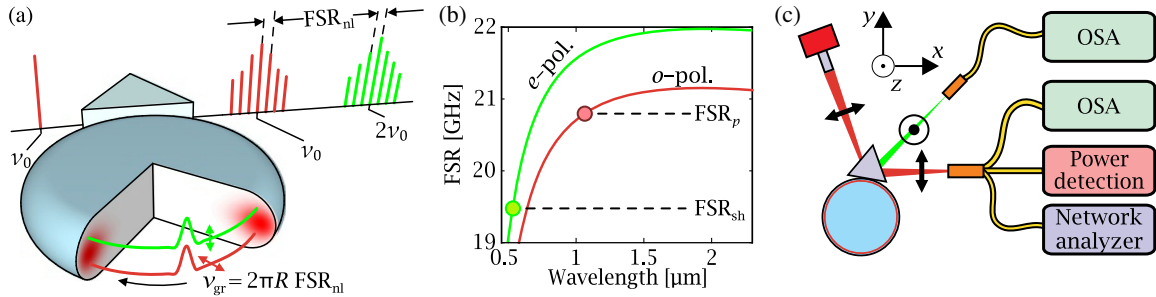


FIG. 1. (a) Continuous-wave near-infrared laser light with frequency ν_0 is prism coupled into a microresonator (radius R). When the phase-matching-criterion for second-harmonic-generation is fulfilled, second-harmonic light at $2\nu_0$ is generated. A sequence of cascaded $\chi^{(2)}$ processes then leads to the buildup of interlocked near-infrared (red spectrum) and visible (green spectrum) combs. In the comb generation regime, the ordinarily (o) polarized pump and extraordinarily (e) polarized second-harmonic waves travel with the same group velocity v_{gr} , associated with the repetition rate equaling the free spectral range FSR_{nl} . (b) FSRs of the microresonator vs wavelength: $FSR_p = 20.8$ GHz and $FSR_{sh} = 19.5$ GHz are the FSRs of the fundamental modes for the pump and second harmonic. (c) Sketch of the experimental setup. OSAs: Optical spectrum analyzers. A detailed description of the experimental procedures is found in [32].

For pump powers exceeding a threshold primary sidebands are generated around the pump and second-harmonic wavelengths. Subsequently, the sideband generation process develops in a cascaded fashion, building up combs around both the pump and second-harmonic frequencies [Fig. 1(a)]. Some prior modeling of these processes in second-harmonic and down-conversion arrangements can be found in [21,29–31]. For the microresonator used, the free spectral ranges (FSRs) at the pump and second-harmonic frequencies are $FSR_p = 20.8$ GHz and $FSR_{sh} = 19.5$ GHz for the fundamental modes [Fig. 1(b)]. The values are very similar for higher-order modes, which are thus not considered [32]. When generating comb structures, however, the FSRs of the combs around the pump and second-harmonic lock to the same nonlinear FSR, FSR_{nl} , corresponding to a shared repetition rate (group velocity) at both frequencies [Fig. 1(a)] as demonstrated numerically and experimentally [Fig. 1(c)] below. The quality factor at the pump frequency is determined to be $Q = 2.8 \times 10^8$ in the coupling regime used [36], while Q is an order of magnitude lower at the second-harmonic frequency [37]. The maximum coupling efficiency [36] is $K_{max} = 0.18$, limited by imperfect spatial mode overlap. Thus, with the laser pump power at 10.3 mW, the maximum incoupled pump power is $K_{max} \times 10.3 \text{ mW} \approx 1.9 \text{ mW}$. When the laser frequency is reduced, the pump resonance shifts through the interplay of thermal and nonlinear effects [Fig. 2(a)] [38], effectively stretching the frequency detunings relative to the cold-cavity reference. We observe multiple comb states, marked (a1), (a2), and (a3) in Fig. 2 while performing a scan. At (a1), only four spectral sidebands can be observed at the pump and second-harmonic wavelengths. The spacing of these sidebands at both the pump and second-harmonic is approximately 416 GHz, corresponding to 20 FSRs of the resonator at the pump wavelength, FSR_p . Thus, the FSR of the comb spectrum even

at the second-harmonic locks to a value close to the pump FSR, i.e., $FSR_{nl} \simeq FSR_p$. This is striking, considering the large FSR offset of 1.3 GHz [Fig. 1(b)] that would accumulate to a noticeable ≈ 26 GHz across 20 modes of the resonator [Figs. 2(b) and 2(c)]. While FSR locking was observed in a bow-tie cavity earlier [26], there, it was not possible to determine whether the waves lock to the pump or second-harmonic FSR due to the very small offset. Thus, this is, we believe, the first time this is determined and furthermore the first observation of an FSR-locked fundamental-to-second-harmonic microresonator-based frequency comb generated solely due to $\chi^{(2)}$ nonlinearities. The next frequency range (a2), around the smaller laser frequency $\Omega = 2\pi\nu_0$, corresponds to much broader, 2-THz-wide, near-infrared, and green spectra [Fig. 2(a2)]. Similar spectra are also observed in the (a3) range. A close-up of Fig. 2(a3) (top) reveals the individual peaks being separated by ≈ 20.8 GHz, which is very close to the linear FSR_p at the pump wavelength. Thus, the obtained comb consists of about 100 individual comb lines. We also observe a broad spectrum around the second-harmonic frequency [Fig. 2(a3) (bottom)]. However, in this case, due to the limited resolution of the OSA employed, the individual comb lines cannot be resolved and the FSR locking is confirmed only in numerical simulations [Figs. 4(c) and 4(f)].

We proceed with introducing a more theoretical insight into the mechanisms leading to comb generation in our system. Spectral data in Fig. 2(a1) suggest that we are dealing with modulation-instability (MI) induced spectral broadening. This is confirmed by the observation of low-frequency rf noise [32] similar to MI in Kerr-combs [39]. The MI in our context is interpreted as the generation of selected resonator modes detuned away from the pump. In particular, through the MI analysis we estimate the sideband mode numbers $M = m_{p,s} \pm \mu$ that acquire

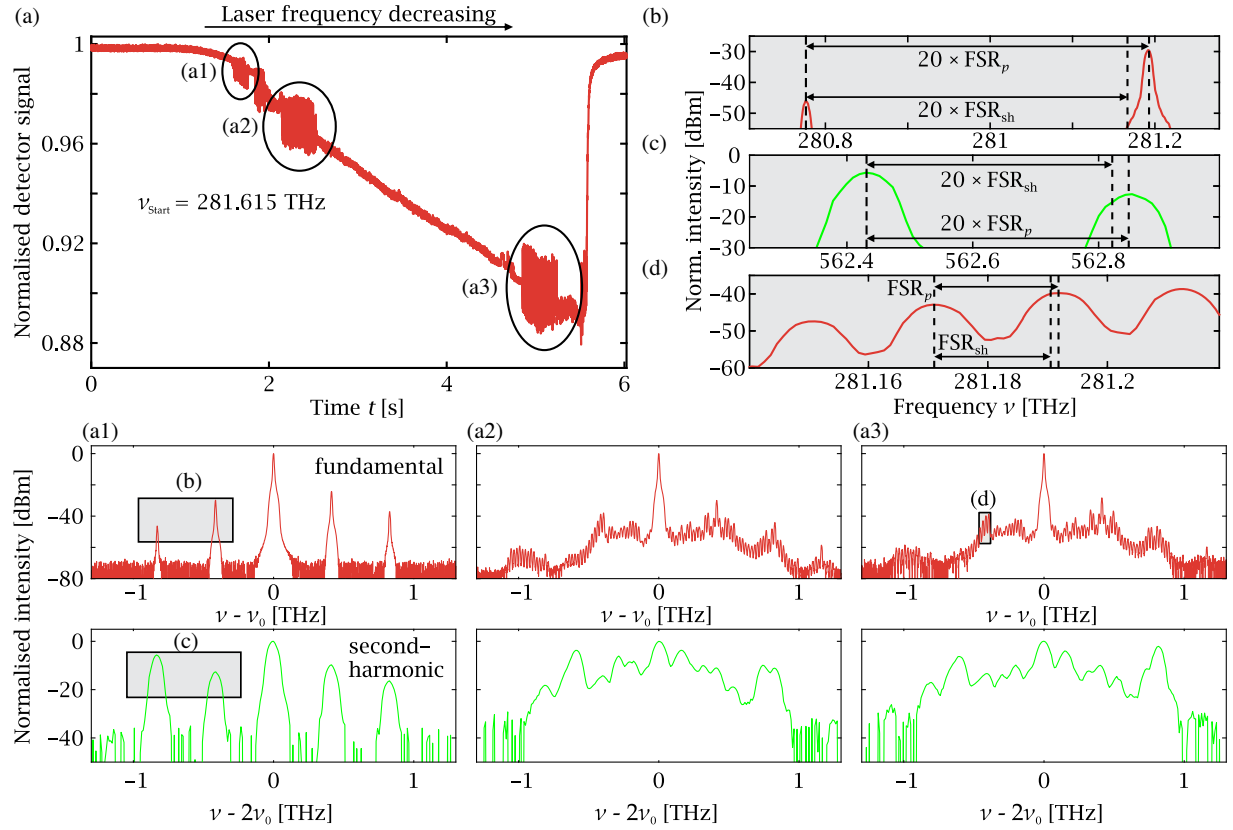


FIG. 2. (a) Slow scan of the pump laser frequency Ω across the pump mode used for comb generation. Reducing $\Omega = 2\pi\nu_0$ reveals comb generation areas marked (a1), (a2), and (a3). At (a1), we observe four sidebands separated by $\approx 20 \times \text{FSR}_p$ around the pump (displayed in red) and second-harmonic (displayed in green) frequencies. Bringing Ω into the (a2) range reveals dense quasicontinua of modes simultaneously generated around the pump and second-harmonic frequencies. With further reduction of the frequency the system enters a quasistationary state, which is replaced again by the dense quasicontinua in the (a3) range. Subsequently the resonance is lost. (b),(c),(d) A close-up revealing the individual peaks of the sparse spectra being separated by $\approx 20 \times \text{FSR}_p$ at both the pump (b) and the second harmonic (c). Quasicontinuous spectra at the pump frequency reveal the separation of neighboring lines by $\approx \text{FSR}_p$ (d), while at the second harmonic the OSA does not allow to resolve features on the FSR scale.

maximal growth rates [32]. Here m_p is a mode number corresponding to the cold resonator frequency ω_p that is nearest the laser frequency Ω , $m_s = 2m_p$ and μ is the mode number offset. When sidebands grow appreciably, they start serving as effective pumps themselves triggering a cascade of up- and down-conversion events between the near-infrared and green spectra. This is the mechanism leading to comb generation. Figure 3 shows the calculated MI-growth rate as a function of the cold resonator detuning $\delta = \omega_p - \Omega$ with the maximally unstable μ being $\pm 20, \pm 21, \pm 22$. In particular, $\mu = 20$ corresponds to the first spectra measured during the experimental scan. This state is characterized by line separation of $\approx 20 \times \text{FSR}_{\text{nl}}$ [Fig. 2(a1)]. For larger δ the MI gain disappears and then reappears with $\mu = 21$ becoming most unstable; modal indices continue to alternate with increasing δ until the resonance is lost (Fig. 3). While MI-analysis explains how combs are triggered, dynamical modeling of the full nonlinear system is required to check the generated spectral shapes after many resonator round-trips. Within the MI

intervals of δ we numerically generate spectra qualitatively and quantitatively similar to the experimental ones and in the same sequential order (Fig. 4). In the $\mu = 20$ interval centered at $\delta \approx 0$, the near-infrared and green comb spectra have four sparse sidebands separated by $\approx 20 \times \text{FSR}_{\text{nl}}$. In the $\mu = 21$ and $\mu = 22$ intervals, the comb spectra become quasicontinuous and extend over ≈ 2 -THz bandwidth. For $\delta \gtrsim 3$ MHz no comb spectra are observed. Alternating stable and unstable detuning intervals [cf. experimental Fig. 2(a) and numerical Fig. 4(a)] with discretely varying μ s unambiguously indicate the field dynamics in a micro-resonator being strongly influenced by the relative sparsity of its spectrum that has finesse order of 10^4 . Previous studies of MI inside hundred times denser spectra in $\chi^{(2)}$ cavities with finesse $\sim 10^2$ [26,40] did not exhibit stability intervals between MI bands corresponding to successive μ s.

The sparse spectra [Figs. 2(a1), 4(b), and 4(c)] correspond to weakly modulated nonlinear periodic wave trains in real space associated with so-called Turing roll patterns (Supplemental Material [32], Figs. 1–3). These types of

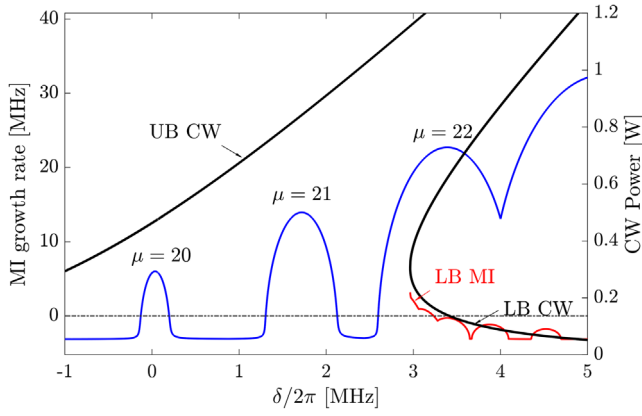


FIG. 3. Blue line shows the modulation-instability (MI) growth rate of the upper branch (UB) of the intracavity cw state against the cold-cavity detuning $\delta = \omega_p - \Omega$. $\mu = \pm 20, \pm 21, \pm 22$ are the mode number offsets with the highest gain within a given interval of δ s. μ s are counted left and right from the mode number $m_p = 13112$ corresponding to the cavity resonance ω_p nearest the pump frequency Ω . $\mu = \pm 20$ matches the experimentally observed spectral lines separated by ≈ 20 FSR. Bold black lines and the right vertical axis show the peak power of the intracavity pump cw state vs δ . The bistability interval starts from $\delta/(2\pi) \approx 3$ MHz and extends towards larger δ s. Red line shows MI-growth rate of the lower branch (LB) of the bistability loop. The dashed horizontal line indicates zero of the MI gain. One can see that LB is stable through most of its existence range. Full details of the parameter values used are provided in [32].

patterns were extensively studied recently in Kerr microresonators [41–43]. An important and distinct feature of the $\chi^{(2)}$ Turing patterns reported by us is that they correspond to a two-color signal with components that are inherently connected nonlinearly and at the same time spectrally separated by an octave. The linear cavity repetition rate varies substantially from one spectral end to another.

However, nonlinear effects can compensate for this difference. Indeed, we can numerically resolve both sparse and quasicontinuous spectra and find the same FSR_{nl} for the near-infrared and green spectra, such that $\text{FSR}_p - \text{FSR}_{\text{nl}} \approx 1$ MHz. This means that the FSR is locked to a value shifted slightly from FSR_p and very significantly, by ≈ 1.3 GHz, from FSR_{sh} . This asymmetry is largely due to the pump power being much higher than the second-harmonic power. The real-space wave trains associated with the quasicontinua in the $\mu = 21, 22$ intervals emerge through the destabilization of Turing patterns and have much deeper modulations of the field intensity (Supplemental Material [32], Fig. 2). Despite this, the locking of FSRs to FSR_{nl} also appears to persist for the quasicontinuous spectra. If δ values are outside the bistability of the homogeneous intracavity state, $\delta/2\pi \lesssim 3$ MHz (Fig. 3), the continua persist indefinitely since they have no alternative state to transform into. As soon as the system becomes bistable, however, a stable low-amplitude state serves as a strong attractor that quickly drags the system outside the continuum and into a low- and constant-intensity stable operation regime. The latter corresponds to the abrupt loss of the resonance in the experimental measurements and modeling.

FSR locking across the octave may appear counterintuitive at first glance. However, it is expected for weakly modulated Turing patterns. Indeed, for a constant-amplitude solution the repetition rates (FSRs) lose their relevance. Hence, for weakly modulated wave trains, the nonlinearity and dissipation-induced locking effects should allow to shift FSR_{sh} to the pump value. While FSR-locking mechanisms for Turing patterns require further detailed studies, this effect was studied for short solitonic pulses in an intracavity OPO [44]. There, it was demonstrated only for angular velocity mismatches comparable to the

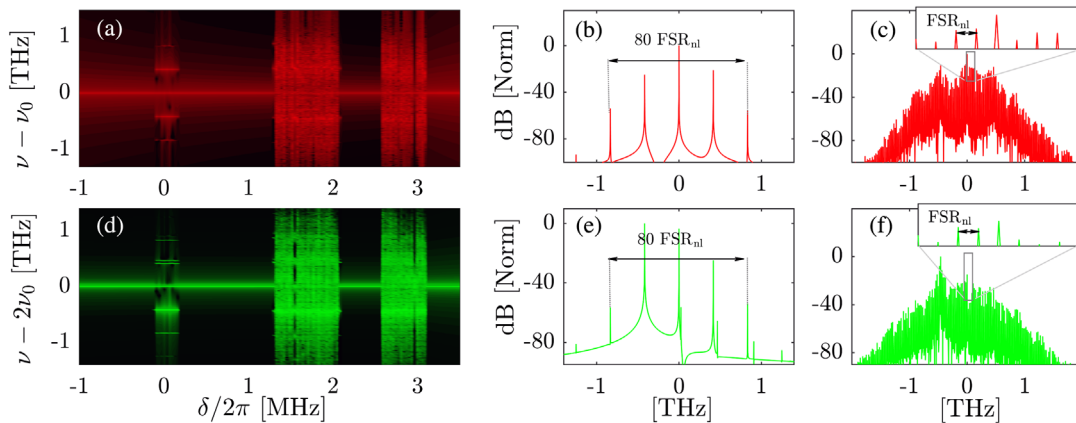


FIG. 4. Top (bottom) row is for the pump (red) [second-harmonic (green)] field. (a),(d) Numerically calculated spectra for a varying detuning δ showing three intervals of comb generation. (b),(e) show the near-infrared and green spectra for $\delta/2\pi = 0.0699$ MHz from (a) and (d), respectively. (c),(f) show the spectra for $\delta/2\pi = 2.6189$ MHz. Enlarged areas show the individual resonances in the quasicontinua separated by FSR_{nl} for both the near-infrared and green spectra. To achieve the spectral states shown here the number of resonator round-trips used was 208 000.

nonlinear linewidth of the cold cavity (\sim few to tens of MHz here) [44], much less than the ~ 1 GHz velocity mismatch relevant for us here.

The results presented here can be considered a first step towards unveiling the full potential of microresonator-based $\chi^{(2)}$ combs; it should be noted that other groups also work on similar experiments [45]. While there is room for improvement, this new approach comes with the advantage of using the generally stronger $\chi^{(2)}$ nonlinearities as opposed to $\chi^{(3)}$ nonlinearities commonly used in microresonator-based combs. We observe combs at pump powers of 2 mW, while first cascaded processes are observed at even lower pump powers of 90 μ W already as internally pumped OPO sets in analogously to bow-tie cavities [25]. Our comb thresholds are on the same order of magnitude as highly optimized Kerr combs [46–48] While we do not show a soliton comb as we are very far from the anomalous dispersion regime [Fig. 1(b)], several theoretical studies argue that it is possible to generate a soliton comb with this scheme provided the phase matching is accompanied by a reduced or vanishing FSR offset between the pump and second harmonic [21,31,44,49]. Matching FSRs spectrally separated by an octave are found in the present sample: in this case, a quasi-phase-matching (QPM) structure has to be employed [36]. Introducing a QPM structure allows for great flexibility regarding the center wavelengths and polarization states of the generated combs. While we use hand-polished microresonators, this method can also be employed for batch-compatible chip-integrated microresonators. Recently, the first chip-integrated OPO was demonstrated, potentially paving the way for chip-integrated $\chi^{(2)}$ microcombs [50]. This would increase the scalability of the platform introduced here, making it even more appealing for applications. Thus, we expect this proof-of-principle device to initiate significant research activities.

This work was supported by the Fraunhofer and Max Planck Cooperation Programme and by the Horizon 2020 Framework Programme (812818, MICROCOMB). Y. M. appreciates the support by a Gisela and Erwin Sick Fellowship. D. V. S. and A. V. are supported by the Leverhulme Trust (RPG-2015-456). The authors would like to thank H. Giessen (University of Stuttgart) for support regarding experimental equipment. J. S. conceived, designed, and set up the experiment, analyzed the data and prepared the figures. Y. M. and L. R. manufactured the microresonator and helped set up the experiment. D. V. S. conceived the governing equations. D. N. P., A. V., and D. V. S. designed codes, performed numerical modelling, analyzed numerical and experimental data and prepared the figures. D. N. P. identified model parameters leading to a good match between numerical and experimental data. J. S., K. B., I. B., and D. V. S. wrote the manuscript. K. B., I. B., and D. V. S. supervised the project.

*karsten.buse@ipm.fraunhofer.de

†d.v.skryabin@bath.ac.uk

- [1] S. A. Diddams *et al.*, An optical clock based on a single trapped $^{199}\text{Hg}^+$ ion, *Science* **293**, 825 (2001).
- [2] N. R. Newbury, Searching for applications with a fine-tooth comb, *Nat. Photonics* **5**, 186 (2011).
- [3] N. Picqué and T. W. Hänsch, Frequency comb spectroscopy, *Nat. Photonics* **13**, 146 (2019).
- [4] A. L. Gaeta, M. Lipson, and T. J. Kippenberg, Photonic-chip-based frequency combs, *Nat. Photonics* **13**, 158 (2019).
- [5] M. Kues, C. Reimer, J. M. Lukens, W. J. Munro, A. M. Weiner, D. J. Moss, and R. Morandotti, Quantum optical microcombs, *Nat. Photonics* **13**, 170 (2019).
- [6] T. Herr, V. Brasch, J. D. Jost, C. Y. Wang, N. M. Kondratiev, M. L. Gorodetsky, and T. J. Kippenberg, Temporal solitons in optical microresonators, *Nat. Photonics* **8**, 145 (2014).
- [7] V. Brasch, M. Geiselmann, T. Herr, G. Lihachev, M. H. P. Pfeiffer, M. L. Gorodetsky, and T. J. Kippenberg, Photonic chip-based optical frequency comb using soliton Cherenkov radiation, *Science* **351**, 357 (2016).
- [8] P. Del’Haye, A. Schliesser, O. Arcizet, T. Wilken, R. Holzwarth, and T. J. Kippenberg, Optical frequency comb generation from a monolithic microresonator, *Nature (London)* **450**, 1214 (2007).
- [9] Y. K. Chembo, D. V. Strekalov, and N. Yu, Spectrum and Dynamics of Optical Frequency Combs Generated with Monolithic Whispering Gallery Mode Resonators, *Phys. Rev. Lett.* **104**, 103902 (2010).
- [10] T. J. Kippenberg, R. Holzwarth, and S. A. Diddams, Microresonator-based optical frequency combs, *Science* **332**, 555 (2011).
- [11] T. Hansson, D. Modotto, and S. Wabnitz, Dynamics of the modulational instability in microresonator frequency combs, *Phys. Rev. A* **88**, 023819 (2013).
- [12] T. J. Kippenberg, A. L. Gaeta, M. Lipson, and M. L. Gorodetsky, Dissipative Kerr solitons in optical microresonators, *Science* **361**, eaan8083 (2018).
- [13] S. J. Herr, V. Brasch, J. Szabados, E. Obrzud, Y. Jia, S. Lecomte, K. Buse, I. Breunig, and T. Herr, Frequency comb up- and down-conversion in synchronously driven $\chi^{(2)}$ optical microresonators, *Opt. Lett.* **43**, 5745 (2018).
- [14] J. S. Levy, M. A. Foster, A. L. Gaeta, and M. Lipson, Harmonic generation in silicon nitride ring resonators, *Opt. Express* **19**, 11415 (2011).
- [15] A. Billat, D. Grassani, M. H. P. Pfeiffer, S. Kharitonov, T. J. Kippenberg, and C.-S. Brès, Large second harmonic generation enhancement in Si_3N_4 waveguides by all-optically induced quasi-phase-matching, *Nat. Commun.* **8**, 1016 (2017).
- [16] E. Timurdogan, C. V. Poulton, M. J. Byrd, and M. R. Watts, Electric field-induced second-order nonlinear optical effects in silicon waveguides, *Nat. Photonics* **11**, 200 (2017).
- [17] X. Guo, C.-L. Zou, H. Jung, Z. Gong, A. Bruch, L. Jiang, and H. X. Tang, Efficient Generation of a Near-Visible Frequency Comb Via Cherenkov-like Radiation from a Kerr Microcomb, *Phys. Rev. Applied* **10**, 014012 (2018).
- [18] D. J. Wilson, K. Schneider, S. Hönl, M. Anderson, Y. Baumgartner, L. Czornomaz, T. J. Kippenberg, and P. Seidler, Integrated gallium phosphide nonlinear photonics, *Nat. Photonics* **14**, 57 (2020).

- [19] Y. He, Q.-F. Yang, J. Ling, R. Luo, H. Liang, M. Li, B. Shen, H. Wang, K. Vahala, and Q. Lin, Self-starting bi-chromatic LiNbO₃ soliton microcomb, *Optica* **6**, 1138 (2019).
- [20] A. V. Buryak, P. Di Trapani, D. V. Skryabin, and S. Trillo, Optical solitons due to quadratic nonlinearities: From basic physics to futuristic applications, *Phys. Rep.* **370**, 63 (2002).
- [21] A. Villois, N. Kondratiev, I. Breunig, D. N. Puzyrev, and D. V. Skryabin, Frequency combs in a microring optical parametric oscillator, *Opt. Lett.* **44**, 4443 (2019).
- [22] V. Ulvila, C. R. Phillips, L. Halonen, and M. Vainio, Frequency comb generation by a continuous-wave-pumped optical parametric oscillator based on cascading quadratic nonlinearities, *Opt. Lett.* **38**, 4281 (2013).
- [23] V. Ulvila, C. R. Phillips, L. Halonen, and M. Vainio, High-power mid-infrared frequency comb from a continuous-wave-pumped bulk optical parametric oscillator, *Opt. Express* **22**, 10535 (2014).
- [24] I. Ricciardi, S. Mosca, M. Parisi, P. Maddaloni, L. Santamaria, P. De Natale, and M. De Rosa, Frequency comb generation in quadratic nonlinear media, *Phys. Rev. A* **91**, 063839 (2015).
- [25] S. Mosca, I. Ricciardi, M. Parisi, P. Maddaloni, L. Santamaria, P. De Natale, and M. De Rosa, Direct generation of optical frequency combs in $\chi^{(2)}$ nonlinear cavities, *Nanophotonics* **5**, 316 (2016).
- [26] S. Mosca, M. Parisi, I. Ricciardi, F. Leo, T. Hansson, M. Erkintalo, P. Maddaloni, P. De Natale, S. Wabnitz, and M. De Rosa, Modulation Instability Induced Frequency Comb Generation in a Continuously Pumped Optical Parametric Oscillator, *Phys. Rev. Lett.* **121**, 093903 (2018).
- [27] R. Ikuta, M. Asano, R. Tani, T. Yamamoto, and N. Imoto, Frequency comb generation in a quadratic nonlinear waveguide resonator, *Opt. Express* **26**, 15551 (2018).
- [28] J. U. Fürst, D. V. Strelakov, D. Elser, M. Lassen, U. L. Andersen, C. Marquardt, and G. Leuchs, Naturally Phase-Matched Second-Harmonic Generation in a Whispering-Gallery-Mode Resonator, *Phys. Rev. Lett.* **104**, 153901 (2010).
- [29] T. Hansson, F. Leo, M. Erkintalo, J. Anthony, S. Coen, I. Ricciardi, M. De Rosa, and S. Wabnitz, Single envelope equation modeling of multi-octave comb arrays in microresonators with quadratic and cubic nonlinearities, *J. Opt. Soc. Am. B* **33**, 1207 (2016).
- [30] T. Hansson, P. Parra-Rivas, M. Bernard, F. Leo, L. Gelens, and S. Wabnitz, Quadratic soliton combs in doubly resonant second-harmonic generation, *Opt. Lett.* **43**, 6033 (2018).
- [31] A. Villois and D. V. Skryabin, Soliton and quasi-soliton frequency combs due to second harmonic generation in microresonators, *Opt. Express* **27**, 7098 (2019).
- [32] See the Supplemental Material at <http://link.aps.org/supplemental/10.1103/PhysRevLett.124.203902> for a full list of parameters used for theoretical modeling and an in-depth description of the experimental methods, which includes Refs. [33–35].
- [33] X. Hu, Y. Liu, X. Xu, Y. Feng, W. Zhang, W. Wang, J. Song, Y. Wang, and W. Zhao, Spatiotemporal evolution of a cosine-modulated stationary field and Kerr frequency comb generation in a microresonator, *Appl. Opt.* **54**, 8751 (2015).
- [34] M. L. Gorodetsky and A. E. Fomin, Geometrical theory of whispering-gallery modes, *IEEE J. Sel. Top. Quantum Electron.* **12**, 33 (2006).
- [35] T. Carmon, L. Yang, and K. J. Vahala, Dynamical thermal behavior and thermal self-stability of microcavities, *Opt. Express* **12**, 4742 (2004).
- [36] I. Breunig, Three-wave mixing in whispering gallery resonators, *Laser Photonics Rev.* **10**, 569 (2016).
- [37] M. Leidinger, S. Fieberg, N. Waasem, F. Kühnemann, K. Buse, and I. Breunig, Comparative study on three highly sensitive absorption measurement techniques characterizing lithium niobate over its entire transparent spectral range, *Opt. Express* **23**, 21690 (2015).
- [38] V. S. Ilchenko and M. L. Gorodetsky, Thermal nonlinear effects in optical whispering gallery microresonators, *Laser Phys.* **2**, 1004 (1992).
- [39] T. Herr, K. Hartinger, J. Riemensberger, C. Y. Wang, E. Gavartin, R. Holzwarth, M. L. Gorodetsky, and T. J. Kippenberg, Universal formation dynamics and noise of Kerr-frequency combs in microresonators, *Nat. Photonics* **6**, 480 (2012).
- [40] F. Leo, T. Hansson, I. Ricciardi, M. De Rosa, S. Coen, S. Wabnitz, and M. Erkintalo, Frequency-comb formation in doubly resonant second-harmonic generation, *Phys. Rev. A* **93**, 043831 (2016).
- [41] J. Pfeifle *et al.*, Optimally Coherent Kerr Combs Generated with Crystalline Whispering Gallery Mode Resonators for Ultrahigh Capacity Fiber Communications, *Phys. Rev. Lett.* **114**, 093902 (2015).
- [42] Z. Qi, S. Wang, J. Jaramillo-Villegas, M. Qi, A. M. Weiner, G. D’Aguanno, T. F. Carruthers, and C. R. Menyuk, Dissipative cnoidal waves (Turing rolls) and the soliton limit in microring resonators, *Optica* **6**, 1220 (2019).
- [43] D. C. Cole, A. Gatti, S. B. Papp, F. Prati, and L. Lugiato, Theory of Kerr frequency combs in Fabry-Perot resonators, *Phys. Rev. A* **98**, 013831 (2018).
- [44] D. V. Skryabin and A. R. Champneys, Walking cavity solitons, *Phys. Rev. E* **63**, 066610 (2001).
- [45] I. Hendry, L. S. Trainor, Y. Xu, S. Coen, S. G. Murdoch, H. G. L. Schwefel, and M. Erkintalo, Experimental observation of internally pumped parametric oscillation and quadratic comb generation in a $\chi^{(2)}$ whispering-gallery-mode microresonator, *Opt. Lett.* **45**, 1204 (2020).
- [46] J. Li, H. Lee, T. Chen, and K. J. Vahala, Low-Pump-Power, Low-Phase-Noise, and Microwave to Millimeter-Wave Repetition Rate Operation in Microcombs, *Phys. Rev. Lett.* **109**, 233901 (2012).
- [47] Y. Xuan *et al.*, High- Q silicon nitride microresonators exhibiting low-power frequency comb initiation, *Optica* **3**, 1171 (2016).
- [48] S. Zhang, J. M. Silver, L. Del Bino, F. Copie, M. T. M. Woodley, G. N. Ghalanos, A. Ø. Svela, N. Moroney, and P. Del’Haye, Sub-milliwatt-level microresonator solitons with extended access range using an auxiliary laser, *Optica* **6**, 206 (2019).
- [49] S. Smirnov, B. Sturman, E. Podivilov, and I. Breunig, Walk-off controlled self-starting frequency combs in $\chi^{(2)}$ optical microresonators, [arXiv:2001.05777](https://arxiv.org/abs/2001.05777).
- [50] A. W. Bruch, X. Liu, J. B. Surya, C.-L. Zou, and H. X. Tang, On-chip $\chi^{(2)}$ microring optical parametric oscillator, *Optica* **6**, 1361 (2019).